

RESEARCH

Open Access



Probiotic-derived amphiphilic exopolysaccharide self-assembling adjuvant delivery platform for enhancing immune responses

Shouxin Sheng^{1†}, Haochi Zhang^{1†}, Xinyu Li^{1†}, Jian Chen^{1,2}, Pu Wang¹, Yanchen Liang¹, Chunhe Li¹, Haotian Li¹, Na Pan¹, Xuemei Bao¹, Mengnan Liu¹, Lixia Zhao², Xiaoyan Li², Pingyuan Guan² and Xiao Wang^{1*}

Abstract

Enhancing immune response activation through the synergy of effective antigen delivery and immune enhancement using natural, biodegradable materials with immune-adjuvant capabilities is challenging. Here, we present NAPS^{L-P} that can activate the Toll-like receptor 4 (TLR4) pathway, an amphiphilic exopolysaccharide, as a potential self-assembly adjuvant delivery platform. Its molecular structure and unique properties exhibited remarkable self-assembly, forming a homogeneous nanovaccine with ovalbumin (OVA) as the model antigen. When used as an adjuvant, NAPS^{L-P} significantly increased OVA uptake by dendritic cells. In vivo imaging revealed prolonged pharmacokinetics of NAPS^{L-P}-delivered OVA compared to OVA alone. Notably, NAPS^{L-P} induced elevated levels of specific serum IgG and isotype titers, enhancing rejection of B16-OVA melanoma xenografts in vaccinated mice. Additionally, NAPS^{L-P} formulation improved therapeutic effects, inhibiting tumor growth, and increasing animal survival rates. The nanovaccine elicited CD4⁺ and CD8⁺ T cell-based immune responses, demonstrating the potential for melanoma prevention. Furthermore, NAPS^{L-P}-based vaccination showed stronger protective effects against influenza compared to Al (OH)₃ adjuvant. Our findings suggest NAPS^{L-P} as a promising, natural self-adjuvanting delivery platform to enhance vaccine design across applications.

Keywords Immune-adjuvant, Exopolysaccharide, Self-assembly, Nanovaccine, Immune response

[†]Shouxin Sheng, Haochi Zhang and Xinyu Li contributed equally to this work.

*Correspondence:

Xiao Wang
wangxiao@imu.edu.cn

¹State Key Laboratory of Reproductive Regulation & Breeding of Grassland Livestock, School of Life Science, Inner Mongolia University, Hohhot 010021, P.R. China

²JinYuBaoLing Biopharmaceutical Co. Ltd, Inner Mongolia 010000, Hohhot, P.R. China



Introduction

Despite extensive efforts to enhance the effectiveness of vaccine adjuvants, the challenge of achieving sufficient immunogenicity persists [1, 2]. Conventional direct immunization with most antigens often leads to inadequate immune responses and rapid clearance of the antigens from the body [3]. To overcome these limitations, adjuvants are employed to enhance immunogenicity, reduce antigen dosage, prolong the prophylactic effect, and accelerate immune responses [4, 5]. However, only a limited number of adjuvants, such as Alum, MF59, virosomes, and montanide ISA-51, have received approval from the US Food and Drug Administration (FDA) [6–8]. Among these, particulate adjuvants based on aluminum salt precipitates (Alum) are the most commonly used, despite their relatively low potency and weak stimulation of cell-mediated immunity [9, 10]. Oil-in-water emulsions containing squalene (MF59 and AS03), as well as liposome-based adjuvant system AS01, are approved for human vaccines, they can occasionally lead to local and mild systemic adverse effects. These effects are generally short-lived and manageable, underscoring the importance of considering their benefits in improving vaccine efficacy and disease prevention [11, 12]. Due to those disadvantages, there is a pressing need to develop novel adjuvants that are both effective and non-toxic for use in organisms.

In recent decades, there have been significant efforts to improve vaccine efficacy through the use of delivery systems and enhanced adjuvants [13, 14]. Biodegradable polymers have emerged as a promising approach, allowing for efficient delivery of antigens encapsulated in nano-vehicles while enhancing immune responses and protecting antigens from degradation. One promising approach is the use of biodegradable polymers as adjuvants, which can encapsulate antigens in nano-vehicles for efficient delivery. These polymers not only enhance immune responses but also protect antigens from degradation. Thus, providing multiple benefits [15–18]. However, the heterogeneity and balance between immune enhancement and biological toxicity of chemical polymers remain challenges for their clinical application.

Natural productions, such as polysaccharides, proteins, and exosomes, as natural building blocks, offer a promising solution to overcome the limitations of synthetic polymers in immunologic adjuvant application [19–21]. Polysaccharides are most used in research due to the high productivity and biodegradability. Recently, polysaccharides-based adjuvants, such as Inulin, chitosan, and alginate, have been reported to possess favorable characteristics of low toxicity and biodegradability [22]. However, the synergy of immune enhancement and delivery properties remains a challenge. For instance, Inulin-derived nanoparticle adjuvants, such as AdvaxTM, have

demonstrated the ability to enhance immune responses in vaccines targeting various viruses, including influenza and hepatitis B, but the poor antigen delivery effects and antigen protective ability limited the synergy effects of Inulin [23]. Moreover, the chitosan and alginate polymers have excellent properties for antigen protection and delivery ability but are not considered immunogenic against influenza whole virus [24, 25]. Overall, natural bio-polymers with synergy immune enhancement and antigen delivery effects remain few reported.

Existing approaches often require the use of coupling agents or activated connectors for antigen modification, which can introduce toxicities and affect the activity of the antigen. Moreover, subsequent purification processes can be inefficient and cumbersome [26]. Another critical concern is the biosafety of vaccine-related nanocarriers. It has been reported that typical cationic carriers like cationic liposomes, chitosan, and PEI can induce cell apoptosis [27]. For instance, charge-reversal functional gold nanoparticles prepared using a layer-by-layer technique have been employed to deliver small interfering RNA (siRNA) and plasmid DNA into cancer cells but exhibit some degree of toxicity towards cell proliferation [28]. Consequently, the development of non-toxic biomaterials with adjuvant activity as antigen delivery systems remains a significant bottleneck.

In this study, we discovered a natural amphiphilic exopolysaccharide named NAPS^{L-p} by screening the self-assembly properties of exopolysaccharides from 139 species of *Lactobacillus*. NAPS^{L-p} was utilized to encapsulate the model antigen OVA, resulting in the formation of nano-sized vaccines that were investigated for their immunostimulatory properties. Non-invasive bioimaging techniques were employed to visualize the pharmacokinetics following systemic administration, while the uptake of particles by dendritic cells was studied using confocal microscopy. The adjuvant capacity of NAPS^{L-p} was assessed by quantifying antibody production and T-cell activity after systemic administration. Moreover, the long-term immunity against B16-melanoma tumors was evaluated by challenging vaccinated mice with tumor cells. Furthermore, the effects of NAPS^{L-p} on influenza protection were examined, and NAPS^{L-p} exhibited stronger protective effects compared to the commonly used Al(OH)₃ adjuvant. Above all, we systematically verified the superior adjuvant capacity and safety of using NAPS^{L-p} for improving vaccine design and performance.

Results

Purification and self-assembly characteristics of NAPS^{L-p}

Natural exopolysaccharides are highly promising candidates for vaccine adjuvants due to their reported self-assembly properties and ability to enhance immunity. In this study, we collected a total of 139 wild bacterial

species, including *Lactobacillus reuteri*, *Lactobacillus helveticus*, *Lactobacillus plantarum*, *Lactobacillus paracasei*, *Lactobacillus delburekii*, and *Lactobacillus rhamnosus*, to identify the best natural exopolysaccharides with self-adjutant potential (Fig. 1a and Supplementary Table 1). The secretory exopolysaccharides were isolated using ethanol precipitation methods, followed by purification through a combination of ion-exchange chromatography and gel permeation chromatography. The resulting purified polysaccharide exhibited excellent homogeneity, as confirmed by the UV spectrum and high-performance gel permeation chromatography profiles (Supplementary Fig. 2 and Fig. 3). To assess the self-assembly properties of the exopolysaccharides, we employed scanning electron microscopy (SEM), dynamic light scattering (DLS), Fourier-transform infrared spectroscopy (FTIR), and liquid chromatography-mass spectrometry (LC-MS) techniques (Supplementary Table 1, Tables 2, and Fig. 1). Among the 139 bacterial species, exopolysaccharides derived from *Lactobacillus plantarum* (EPS-301) demonstrated strong self-assembly properties based on the SEM, FTIR, and DLS results (Supplementary Table 1, Tables 2, and Fig. 1). Further purification of the crude product was performed using DEAE Sepharose fast flow and Sepharose CL-6B gel column chromatography. The morphology of the polysaccharides, as observed under an electron microscope, appeared fibrous (Fig. 1c). Following homogenization, the exopolysaccharides from *Lactobacillus plantarum* self-assembled into spherical nanoparticles with a size of approximately 30 nm at room temperature, exhibiting a bright and relatively homogeneous appearance in water (Fig. 1c and d, and Fig. 1e). Based on these findings, we designated the selected exopolysaccharides as natural self-assembly exopolysaccharides, naming them NAPS^{L-p}.

To further understand the self-assembly behavior of NAPS^{L-p}, we investigated its response to different solvents, including SDS (0.01 M), DMSO, NaOH (0.01 M), and 50% ethanol. The size of NAPS^{L-p} nanoparticles in DMSO were measured to be 26.42 ± 7 nm, which differed from that in water (Fig. 1f and Supplementary Fig. 4a). Similar morphologies were observed in NaOH solutions (Supplementary Fig. 4b), with a reduced size of approximately 24 ± 7 nm for NAPS^{L-p}. When treated with SDS (0.01 M), the morphology of NAPS^{L-p} appeared as a network structure (Supplementary Fig. 4c). In 50% ethanol, the morphology of NAPS^{L-p} exhibited nanofiber structures (Supplementary Fig. 4d), indicating the gel formation of NAPS^{L-p} in 50% ethanol solution. These findings provide insights into the self-assembly behavior of NAPS^{L-p} in different solvents, enhancing our understanding of its properties.

To gain a more detailed understanding of the nanoscale self-assembly mechanism, molecular dynamics (MD)

simulations were performed on NAPS^{L-p} molecules in water. Snapshots were captured at different time points to examine the changes in molecular configuration and self-assembly behavior during the simulation process. As depicted in Fig. 1g and Supplementary Fig. 5a, 30 NAPS^{L-p} molecules were initially randomly distributed in the solution at 0 ns. At 10 ns, some molecules began to aggregate into clusters. Finally, all 30 NAPS^{L-p} molecules clustered together, forming a stable spherical nanocluster at 50 ns. This observation confirmed the spontaneous aggregation behavior of NAPS^{L-p} molecules in aqueous solution.

Several interactive forces play a role in the self-assembly of nanoparticles, including hydrogen bonding, hydrophobic interactions, electrostatic interactions, and van der Waals forces. To investigate these forces, the number of hydrogen bonds formed between the 30 NAPS^{L-p} molecules was calculated throughout the simulation. As shown in Supplementary Fig. 5b, the number of intermolecular hydrogen bonds increased progressively over time, indicating a decrease in the distance between NAPS^{L-p} molecules. Additionally, we analyzed the number of hydrogen bonds between NAPS^{L-p} molecules and water molecules during the simulation, and the results (Supplementary Fig. 5c) revealed a reduction in the hydrogen bonds between NAPS^{L-p} molecules and water molecules. This reduction indicated the tendency of NAPS^{L-p} molecules to self-assemble, with intermolecular hydrogen bonding being one of the primary forces driving molecule aggregation. Furthermore, Fig. 1h illustrates the analysis of the interaction between a NAPS^{L-p} molecule located in the center of a spherical nanocluster and the surrounding NAPS^{L-p} molecules. The figure demonstrates that NAPS^{L-p} molecules primarily self-assemble through the formation of numerous hydrogen bonds between the hydroxyl or carbonyl groups on the molecular chain and the surrounding NAPS^{L-p} molecules.

Hydrophobic interactions between water molecules and hydrophobic groups are another driving force for the self-assembly of nanoparticles. The degree of hydrophobicity can be approximated by the solvent-accessible surface area (SASA). In this study, we analyzed the SASA of the entire system during the simulation process to evaluate the compactness of NAPS^{L-p} molecules in the solution. As shown in Supplementary Fig. 5d, the SASA values of all polysaccharide molecules in the system decreased from 528.715 nm^2 at 0 ns to 372.145 nm^2 at the end of the 50 ns simulation. The system reached stability after 50 ns. The decrease in SASA indicated that the NAPS^{L-p} molecules became more compact, limiting their contact with water molecules. This finding suggests that NAPS^{L-p} molecules aggregate through hydrophobic interactions. The results shed light on the molecular mechanisms underlying the self-assembly process and enhance

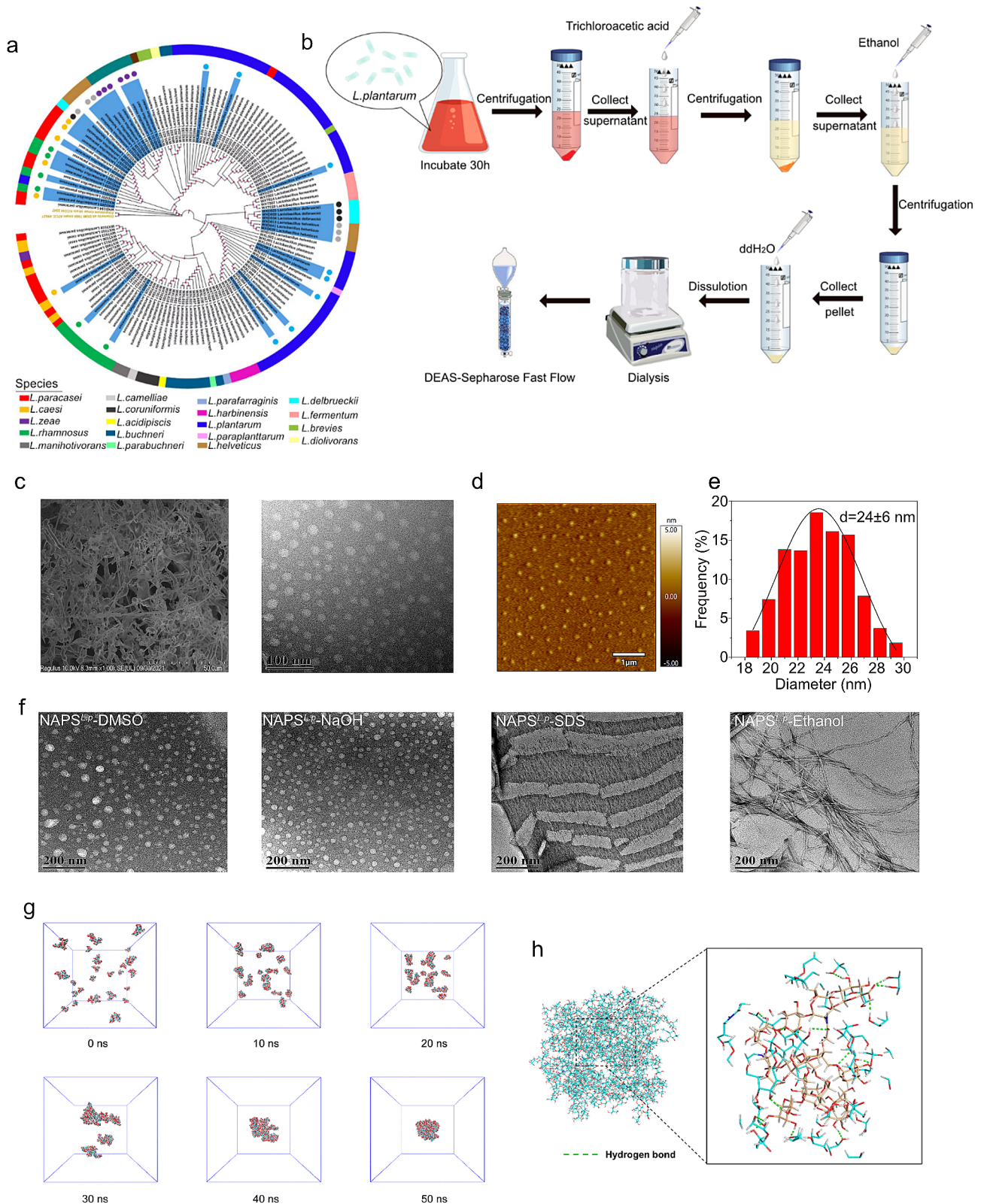


Fig. 1 Screening, isolation, and self-assembly characterizations of NAPS^{L-P}. **(a)** Neighbor join-based phylogenetic tree of the bacteria. **(b)** Generation and isolation of exopolysaccharide from selected bacteria. **(c)** SEM and TEM images of NAPS^{L-P}. SEM image showed the fibrous shape of NAPS^{L-P} in water (left). The TEM image showed the morphology of NAPS^{L-P} after self-assembly inducing. **(d)** AFM image showed the three-dimensional morphology of self-assembled NAPS^{L-P}. **(e)** The size of self-assembled NAPS^{L-P} about 24 ± 6 nm. **(f)** Morphology of self-assembled NAPS^{L-P} in different solutions. **(g)** Snapshots of the MD simulation systems at 0 ~ 50 ns. **(h)** Schematic diagram of the interaction between a NAPS^{L-P} molecule

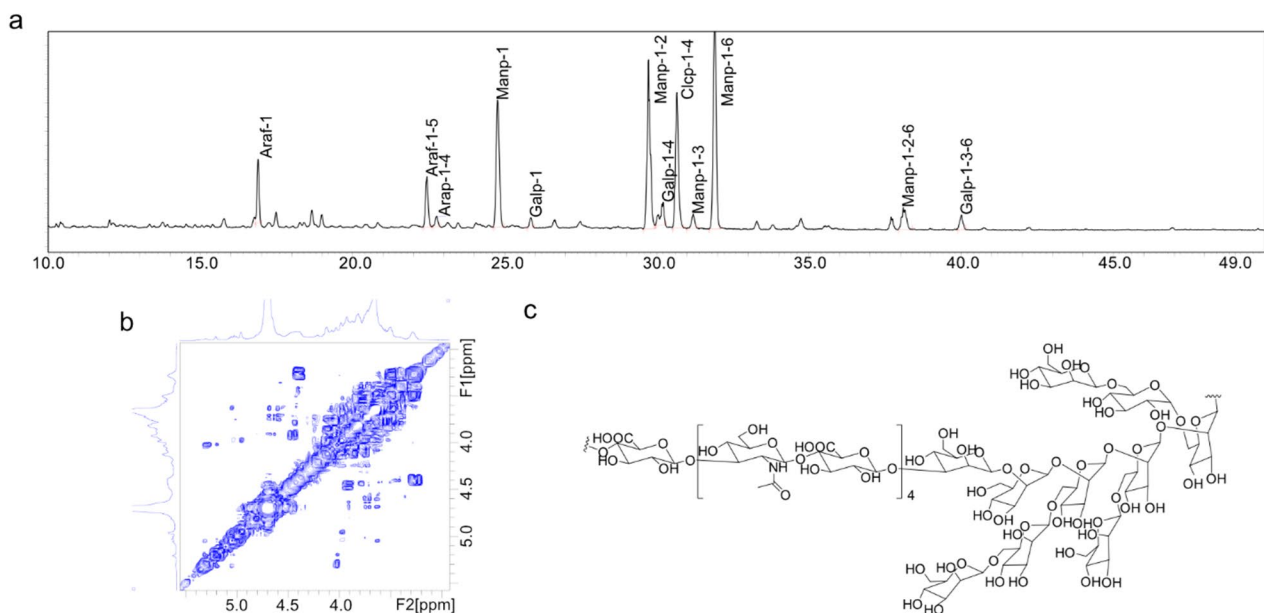


Fig. 2 Chemical structure of $\text{NAPS}^{\text{L-p}}$. (a) LC-MS results of $\text{NAPS}^{\text{L-p}}$. (b) ^1H - ^1H -COSY of $\text{NAPS}^{\text{L-p}}$. (c) Chemical structure of $\text{NAPS}^{\text{L-p}}$ from results of LC-MS and NMR

our understanding of the properties of $\text{NAPS}^{\text{L-p}}$ as a potential self-adjuvant for immunity enhancement.

Molecular structure and characteristics of $\text{NAPS}^{\text{L-p}}$

We assessed the homogeneity and molecular weight of the polysaccharides. The average molecular weight was determined to be approximately 84.3 kDa by calculating the standard dextrans and measuring the elution time of the polysaccharides. The CD spectra of $\text{NAPS}^{\text{L-p}}$ (Supplementary Fig. 6) revealed that the secondary conformational structures of $\text{NAPS}^{\text{L-p}}$ were primarily composed of α -helices and β -sheets. Analysis of the pure polysaccharide composition using high-performance liquid chromatography (HPLC) indicated the presence of galactosamine hydrochloride, arabinose, glucosamine hydrochloride, galactose, glucose, mannose, and glucuronic acid, with a molar ratio of 3.3:1.2:2.1:10.5:1:3.1 (Supplementary Fig. 7).

To gain further insights into the molecular structure of $\text{NAPS}^{\text{L-p}}$, we conducted additional investigations using Fourier transform infrared spectroscopy (FTIR) spectra, X-ray photoelectron spectroscopy (XPS), rheometer tests, and small angle X-ray scattering (SAXS) analysis (Supplementary Figs. 8–11).

We defined the glycoside linkages of polysaccharides by gas chromatography-mass spectrometer (GC-MS) analysis (Fig. 2a and Supplementary Table 3). Twelve sugar residues of the polysaccharides could be elucidated as 2,3,5- Me_3 -Araf, 2,3- Me_2 -Araf, 2,3- Me_2 -Arap, 2,3,4,6- Me_4 -Manp, 2,3,4,6- Me_4 -Galp, 3,4,6- Me_3 -Manp, 2,3,6- Me_3 -Galp, 2,3,6- Me_3 -Glcp, 2,4,6- Me_3 -Manp,

2,3,4- Me_3 -Manp, 3,4- Me_2 -Manp, 2,4- Me_2 -Galp with the molar ratio of 6.4:5.6:1.2:16.6:1:19.2:3.2:15.5:1.7:24.7:3.4:1.5. The corresponding link method is Araf-(1 \rightarrow , \rightarrow 5)-Araf-(1 \rightarrow , \rightarrow 4)-Arap-(1 \rightarrow , Manp-(1 \rightarrow , Galp-(1 \rightarrow , \rightarrow 2)-Manp-(1 \rightarrow , \rightarrow 4)-Galp-(1 \rightarrow , \rightarrow 4)-Glcp-(1 \rightarrow , \rightarrow 3)-Manp-(1 \rightarrow , \rightarrow 6)-Manp-(1 \rightarrow , \rightarrow 2,6)-Manp-(1 \rightarrow , \rightarrow 3,6)-Galp-(1 \rightarrow , respectively. Nuclear magnetic resonance (NMR), including ^1H , DEPT 135, and 2D NMR spectra (^1H - ^1H -COSY, HSQC, HMBC, and NOESY), was further carried out to reveal the $\text{NAPS}^{\text{L-p}}$ structure (Fig. 2b and Supplementary Fig. 12), all glycosidic bond signals were speculated (Supplementary Table 4). Based on the results of glycosidic linkage analysis and NMR spectra analysis, the main chain connection of $\text{NAPS}^{\text{L-p}}$ was \rightarrow 3)- β -D-Galp-(1 \rightarrow 4)- β -D-GlcpNAc-(1 \rightarrow 3)-Man-1 \rightarrow 2-Man-1 \rightarrow 2,6-Man-1 \rightarrow 2,6-Man-1 \rightarrow (Fig. 2c).

Characteristics of $\text{NAPS}^{\text{L-p}}$ @OVA nanoparticles

$\text{NAPS}^{\text{L-p}}$ and OVA were mixed to create the $\text{NAPS}^{\text{L-p}}$ @OVA nanoparticles (Fig. 3a). These nanoparticles had a mean size of 41.32 ± 3.14 nm (PDI: 0.121 ± 0.04) for $\text{NAPS}^{\text{L-p}}$ and 83.98 ± 1.62 nm (PDI: 0.142 ± 0.06) for $\text{NAPS}^{\text{L-p}}$ @OVA, as determined by DLS (Supplementary Table 5). The TEM image showed that $\text{NAPS}^{\text{L-p}}$ @OVA had a uniform spherical shape (Fig. 3b and Fig. 3c). The successful encapsulation of OVA was confirmed by UV-Vis and FTIR spectroscopy. CD spectroscopy revealed the structure of OVA in $\text{NAPS}^{\text{L-p}}$ @OVA remained intact (Fig. 3d, Supplementary Fig. 13 and Fig. 14). The contact angle analysis indicated that both $\text{NAPS}^{\text{L-p}}$ and $\text{NAPS}^{\text{L-p}}$ @

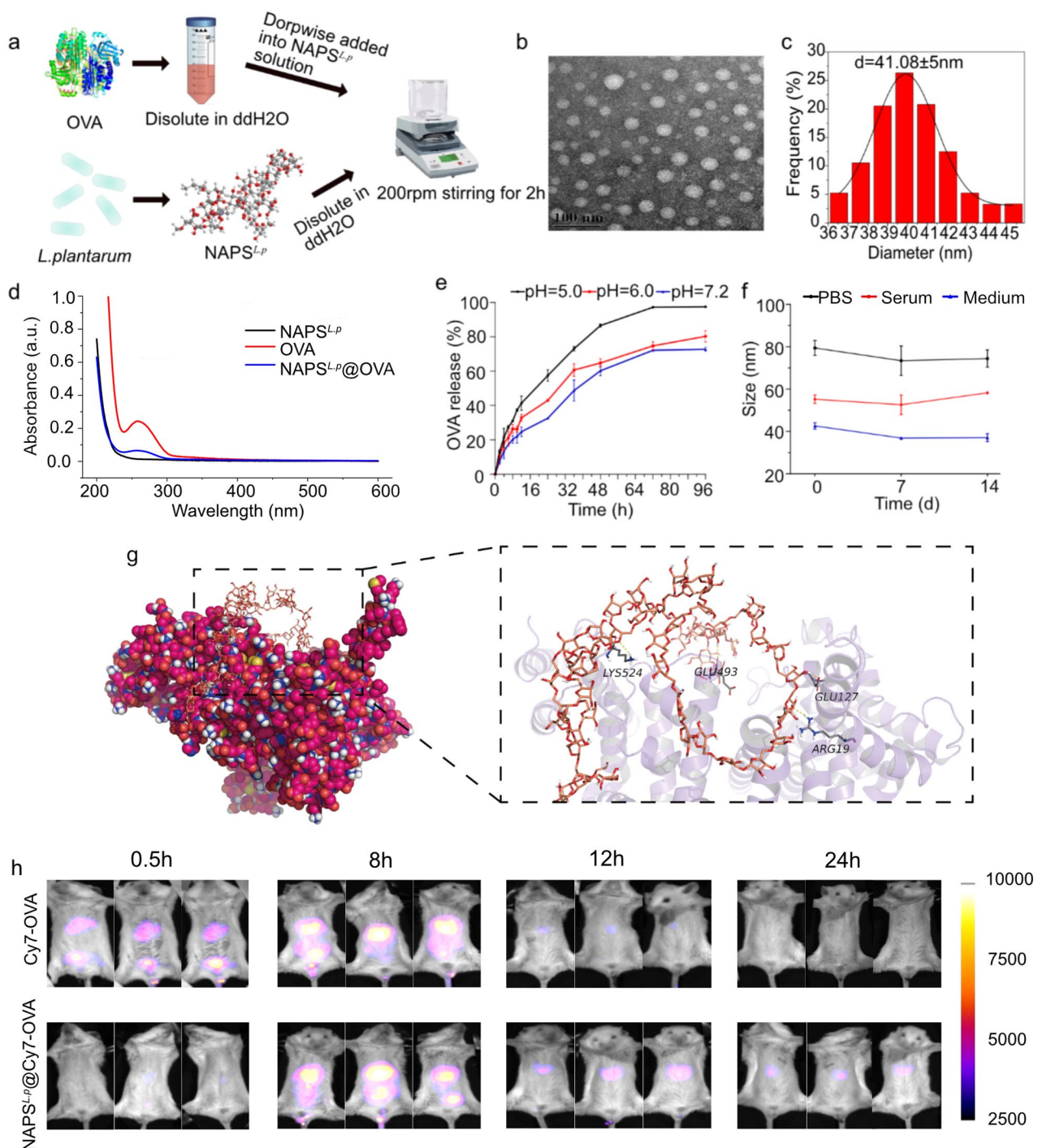


Fig. 3 Characterizations of NAPS^{L-p}@OVA. **(a)** Preparation procedure of NAPS^{L-p}@OVA. **(b)** TEM images of NAPS^{L-p}@OVA. **(c)** Size distributions of NAPS^{L-p}@OVA. **(d)** UV spectrum of NAPS^{L-p}@OVA. **(e)** OVA releasing curve of NAPS^{L-p}@OVA in different pH conditions. **(f)** The stability of NAPS^{L-p}@OVA under various buffer conditions. **(g)** The structure mode of NAPS^{L-p}-OVA. OVA and NAPS^{L-p} are marked in purple and orange, respectively, and NAPS^{L-p} is depicted as a bar (C: orange; H: white; O: red; N: blue; hydrogen bonds: indicated by yellow dotted lines) The bond length is 2.10Å, 2.37Å, 2.43Å, and 2.68Å. **(h)** In vivo fluorescence imaging of Cy7-OVA and NAPS^{L-p}@Cy7-OVA at timed intervals after intravenous injection. The data are presented as mean ± SD ($n = 3$)

OVA exhibited hydrophilicity, enhancing their bioavailability (Supplementary Fig. 15).

NAPS^{L-p}@OVA had an antigen loading capacity of $57.98 \pm 1.65\%$ and an encapsulation efficiency of

$87.30 \pm 2.64\%$ (Supplementary Table 5). Release experiments showed that less than 25% of OVA was released within 24 h at pH 7.2, while at pH 6.0 and 5.5, more than 40% and 60% of OVA were released, respectively (Fig. 3e).

This pH-responsive release indicated that potential for targeted antigen delivery and immune responses [29]. The stability of NAPS^{L-p}@OVA in various solvents, including PBS, serum, and cell medium, was confirmed for 14 days (Fig. 3f). The assembly between NAPS^{L-p} and OVA protein was verified using stoichiometric calculation and molecular docking analysis (Fig. 3g). Four hydrogen bonds were observed between the active site of OVA protein and NAPS^{L-p} segments. The calculated dock score value for NAPS^{L-p}@OVA protein was -7.505 kcal/mol. To assess antigen retention, Cy7-labeled OVA was injected into mice. The fluorescent signal of NAPS^{L-p}@Cy7-OVA was detectable even after 24 h, indicating prolonged antigen retention and stimulation capability for antigen-presenting cells (APCs) (Fig. 3h).

Immunity activation and antigen presentation mediated by NAPS^{L-p}@OVA

Dendritic cells (DCs) were tested for antigen uptake using FITC-labeled OVA (OVA-FITC) or NAPS^{L-p}-bound OVA-FITC (NAPS^{L-p}@OVA-FITC). Results showed that NAPS^{L-p}@OVA-FITC had higher intracellular uptake in BMDCs compared to OVA-FITC alone. Co-localization of NAPS^{L-p}@OVA-FITC with lysosomes in primary dendritic cells was observed (Fig. 4a, and 4b). A hemolysis test evaluated the hemolysis of NAPS^{L-p}@OVA to red blood cells, and the results showed that no significant hemolysis occurred (Supplementary Fig. 16), which indicated good biocompatibility. Cytotoxicity tests on BMDCs and RAW264.7 showed no significant toxicity even at high concentrations (100 $\mu\text{g}/\text{mL}$) of NAPS^{L-p}@OVA (Fig. 4c and Supplementary Fig. 17). NAPS^{L-p}@OVA increased the expression of CD40, CD80, CD86, and MHC II on BMDCs, indicating DC maturation and activation (Fig. 4d-g and Supplementary Fig. 18). As indicated in Fig. 4h and supplementary Fig. 19, we further observed that the treatments of NAPS^{L-p}@OVA increased the expression level of SIINFEKL-H-2K^b complexes on the surface of BMDCs by 2.87-fold compared to the "OVA" group, suggesting the NAPS^{L-p}@OVA nanovaccines efficiently enhance the efficacy of antigen cross-presentation of DCs. The levels of TNF- α , IL-6, IL-12p70, and IL-4 cytokines were higher in the cultural supernatant of BMDCs treated with NAPS^{L-p}@OVA compared to control groups, suggesting cellular and humoral immune response activation (Fig. 4i-l). To investigate the signaling pathway mediated by NAPS^{L-p}, the mRNA transcript levels of TLR4 in DC cells were measured by RT-PCR after exposure of DC cells to various concentrations of NAPS^{L-p}. The results showed that NAPS^{L-p} upregulated TLR4 expression in the DCs cells compared to the control group (Fig. 4m). To confirm further that NAPS^{L-p} exerts its effects through the TLR4 signaling pathway, we used the TLR4 antagonist TAK-242 to determine whether the

NAPS^{L-p}-induced secretion of IL-6 and TNF- α was due to the activation of specific TLR4. As shown in Fig. 4n and o, the least number of cytokines was produced when DC cells were exposed to the medium alone. However, the secretion of TNF- α and IL-6 was significantly inhibited in DC cells pre-incubated with TAK-242 and then added to NAPS^{L-p} compared to the NAPS^{L-p} treatment alone, which further demonstrated that the NAPS^{L-p} activates the TLR4 pathway in BMDC. In addition, Simulated calculation suggested that NAPS^{L-p} binds to TLR4 protein mainly through hydrogen bonds and hydrophobic forces (Fig. 4p). After binding to NAPS^{L-p}, the conformation of the loop region of TLR4 protein will change to a certain extent, thereby activating downstream signaling pathways and exerting its adjuvant activity. Mice were subcutaneously immunized with NAPS^{L-p}@OVA to evaluate humoral immune responses. We specifically analyzed antibodies targeting individual components of the vaccine, focusing on IgG, IgG1, and IgG2b. Notably, both NAPS^{L-p}@OVA and aluminum OVA groups exhibited higher titers of IgG, IgG1, and IgG2b compared to the OVA-treated group (Supplementary Fig. 20), indicating that NAPS^{L-p} encapsulation enhances antibody production and acts as an immune adjuvant. To assess potential in vivo toxicities of NAPS^{L-p}@OVA, we performed hematoxylin and eosin (H&E) staining after a single administration. One week post-administration, mice were sacrificed, and liver, spleen, heart, and lung samples were collected. The results demonstrated that NAPS^{L-p}@OVA did not induce pathological changes (Supplementary Fig. 21), confirming the low toxicity profile of NAPS^{L-p}.

Antitumor effect of the nanovaccines in a subcutaneous tumor model

Mice were vaccinated with B16-OVA melanoma tumor cells to study anticancer immunity. The mice received subcutaneous immunizations of NAPS^{L-p}, OVA₂₅₇₋₂₆₄/CpG@OVA₂₅₇₋₂₆₄, NAPS^{L-p}@OVA₂₅₇₋₂₆₄ and PBS three times at one-week intervals (Fig. 5a). After vaccination, the mice were challenged with B16-OVA melanoma cells. The group treated with CpG@OVA showed inhibited tumor progression compared to the control group injected with PBS. Notably, the NAPS^{L-p}@OVA-treated group exhibited the best therapeutic effect, with significantly prolonged animal survival and complete tumor elimination in three mice (Fig. 5b, c, d). In the CpG@OVA group, 2 out of 10 mice showed complete tumor regression. In comparison, only 1 out of 10 mice in the NAPS^{L-p} group exhibited regression, and no complete regression was observed in the other groups (Fig. 5b). Importantly, the body weights of the vaccinated mice slightly increased, indicating minimal effects on their weight (Fig. 5e). Given the crucial role of immune memory in long-term antitumor benefits, therefore, we investigated

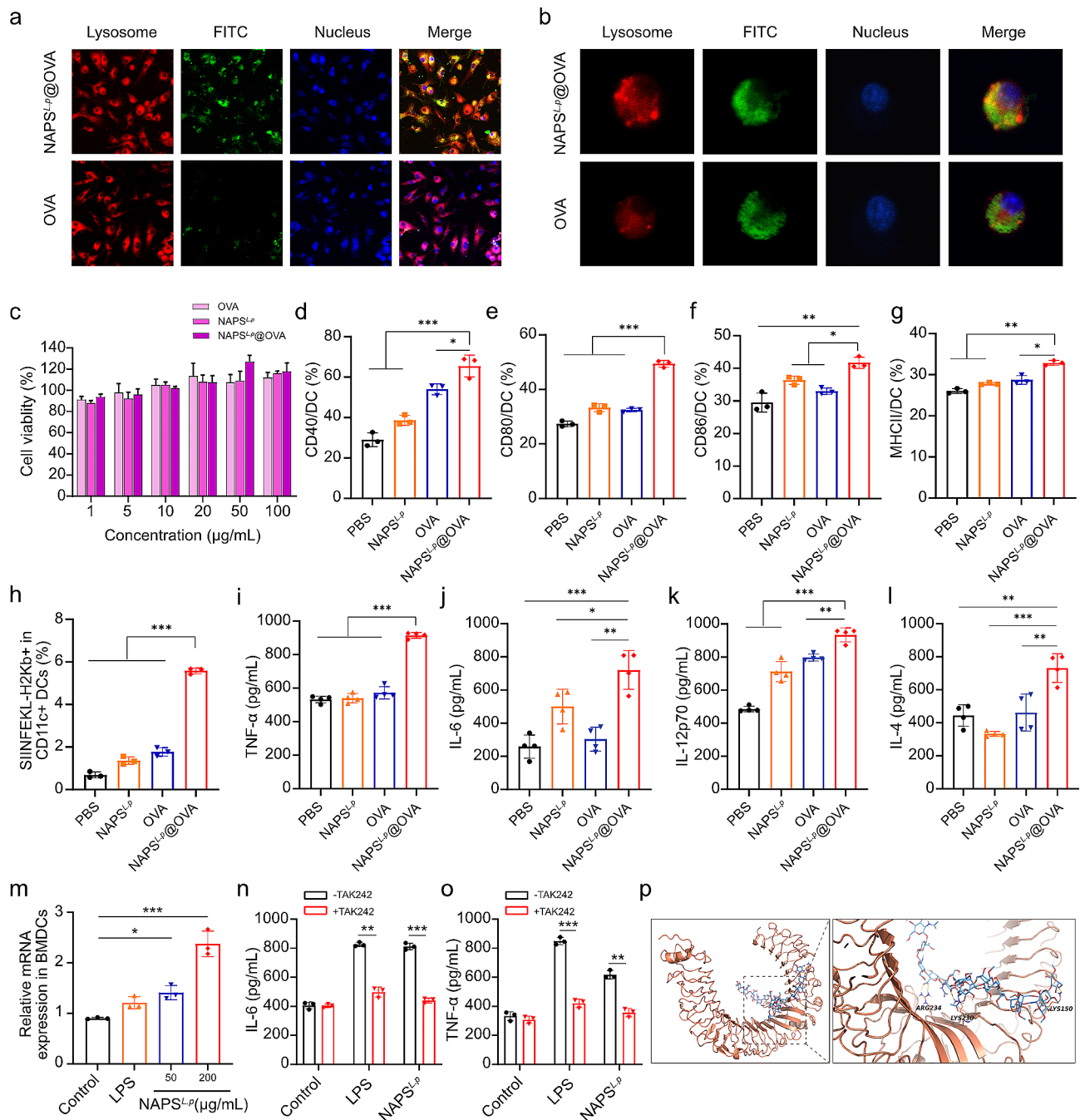


Fig. 4 Immunity activation and antigen presentation mediated by NAPS^{L-p}@OVA. **(a)** Confocal images of primary dendritic cells co-incubating with NAPS^{L-p}@OVA-FITC or FITC-OVA. **(b)** High-resolution images of primary dendritic cells. These results indicated that the FITC-OVA exhibited stronger internalization abilities after NAPS^{L-p} encapsulation. **(c)** Cytotoxicity of BMDCs after coculturing for 24 h with NAPS^{L-p}, OVA and NAPS^{L-p}@OVA. The expression levels of **(d)** CD40, **(e)** CD80, **(f)** CD86, and **(g)** MHC-II, were measured with flow cytometers. **(h)** The percentage of SIINFEKL-H2Kb⁺ on BMDCs treated with NAPS^{L-p}, OVA, and NAPS^{L-p}@OVA. The cytokine secretion levels of **(i)** TNF- α , **(j)** IL-6, **(k)** IL-12p70, and **(l)** IL-4 were measured with ELISA assays. **(m)** The mRNA transcription levels of TLR4 in DCs cells. IL-6 **(n)** and TNF- α **(o)** in the supernatant of DCs were tested by ELISA kit. **(p)** Molecular docking of NAPS^{L-p} and TLR4. The data are presented as mean \pm SD ($n = 3$). One-way ANOVA with a Tukey multiple comparisons test was used for statistical analysis. *, $p < 0.05$; **, $p < 0.01$; ***, $p < 0.001$

the persistence of immune memory in vivo after vaccination with NAPS^{L-p}@OVA_{257–264}. As indicated in Fig. 5f and g, we investigated the immune memory T cells in the spleens on day 60 since the fast immunization by

flow cytometry. It is worth noting the proportions of T_{EM} (CD3⁺ CD8⁺ CD44⁺ CD62L⁻) and T_{CM} (CD3⁺ CD8⁺ CD44⁺ CD62L⁺) in the mice immunized with NAPS^{L-p}@OVA reveals a 4.70-fold and 2.10-fold increase, compared

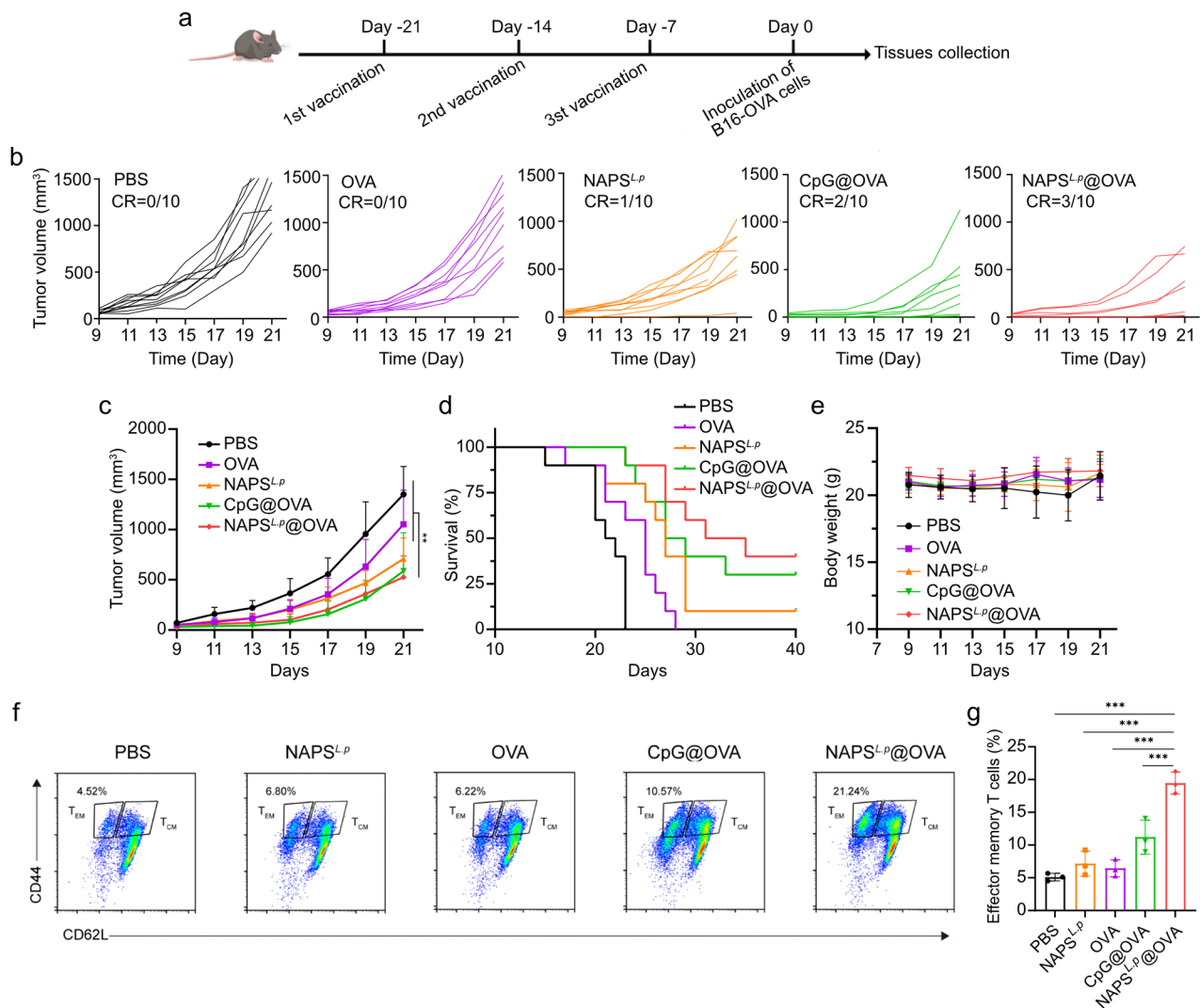


Fig. 5 Anti-tumor efficacy of prophylactic immunization in a subcutaneous B16-OVA melanoma model. **(a)** Schematic illustration of prophylactic immunization for subcutaneous B16-OVA melanoma model. **(b)** Individual tumor growth curves for mice after different treatments. **(c)** Growth curves of the average volumes in the indicated groups ($n = 10$). **(d)** Survival curves of mice with different treatments as indicated ($n = 10$). **(e)** Body weight changes of mice in different groups ($n = 10$). **(f)** Representative scatter plots and gating information derived from analysis of effector memory T cells (T_{EM} , $CD3^+ CD8^+ CD44^+ CD62L^-$) cells in Spleen. **(g)** Quantitative analysis of T_{EM} cells in Spleen ($n = 3$). Data are shown as mean \pm SD. One-way ANOVA with a Tukey multiple comparisons test was used for statistical analysis. **, $p < 0.01$, ***, $p < 0.001$

with that in the control group (Fig. 5f, g and Supplementary Fig. 22). Furthermore, NAPS^{L-p}@OVA vaccination induced the greatest increase in tissue resident memory T cells compared with those in the other groups (Supplementary Fig. 23). These results demonstrated that the NAPS^{L-p}@OVA nanovaccines can generate sustained antigen-specific immune memory effect for preventing antigen-specific tumor occurrence.

The efficacy of NAPS^{L-p}@OVA_{257–264} was evaluated in mice with B16-OVA melanoma. Mice were divided into five groups and received different treatments (Fig. 6a). The tumor inhibition rates were 2.04%, 38.25%, 40.93%, 62.95%, and 80.45% for PBS, NAPS^{L-p}, OVA_{257–264}, CpG@OVA_{257–264}, and NAPS^{L-p}@OVA_{257–264} groups,

respectively (Fig. 6e). NAPS^{L-p}@OVA showed the highest inhibition, but all vaccine formulations inhibited tumor growth (Supplementary Fig. 24 and Fig. 6b, d). NAPS^{L-p}@OVA also prolonged animal survival (Fig. 6c) without causing weight loss (Supplementary Fig. 25).

Tumor-infiltrating immune cells were analyzed, and the NAPS^{L-p}@OVA groups showed significantly increased $CD3^+ CD4^+$ and $CD3^+ CD8^+$ T cell infiltration in tumor tissues compared to the control group (Fig. 6f, g and Supplementary Figs. 26, 27). NAPS^{L-p}@OVA vaccination effectively reduced regulatory T cells (Tregs, $CD3^+ CD4^+$ Foxp3⁺ T cells) and myeloid-derived suppressor cells (MDSCs, $CD11b^+ Gr-1^+$) in tumor tissues (Fig. 6h, i and Supplementary Figs. 28, 29). Additionally, NAPS^{L-p}@

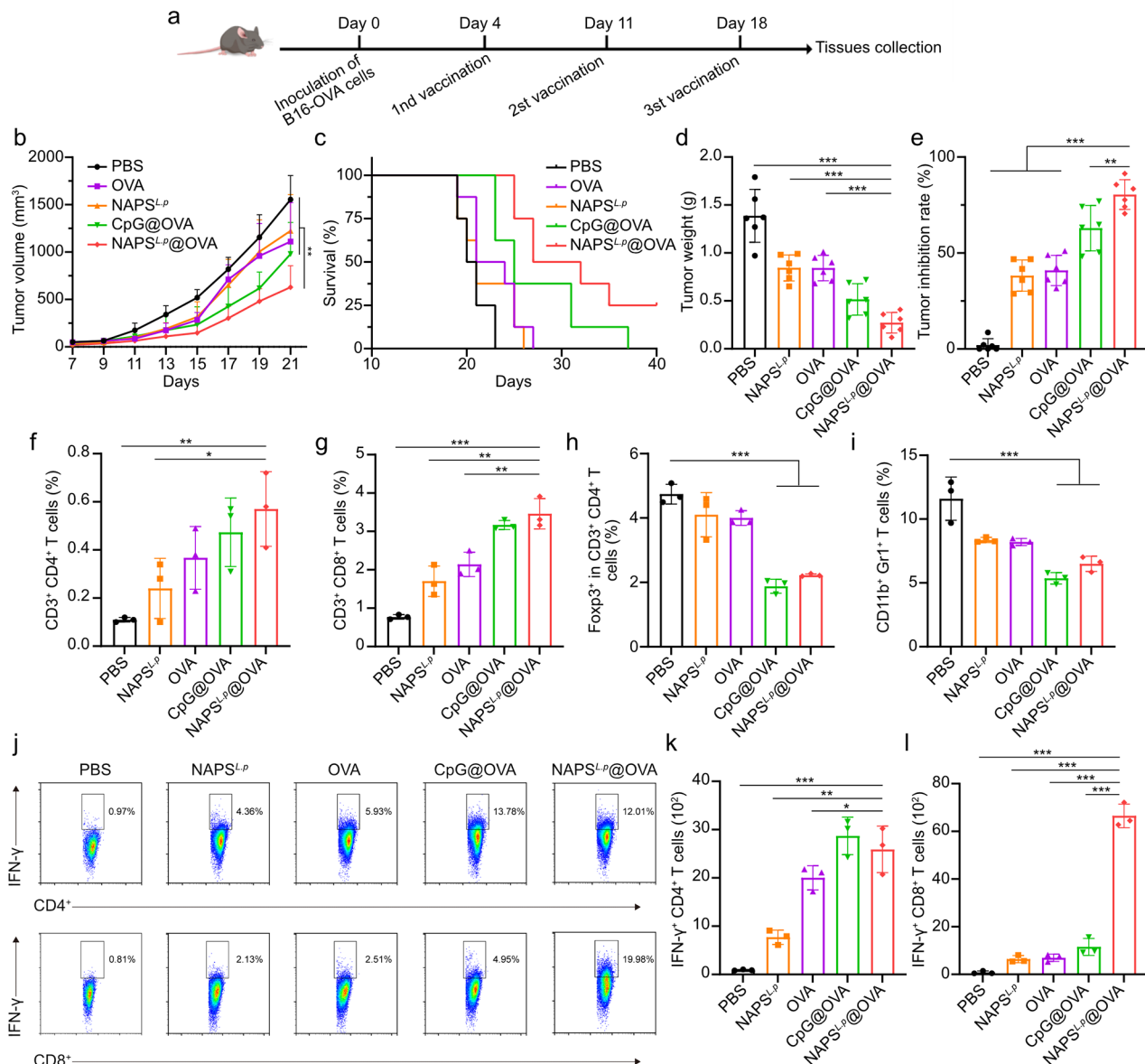


Fig. 6 Anti-tumor efficacy in a B16-OVA melanoma tumor model. **(a)** Schematic illustration of therapeutic immunization for subcutaneous B16-OVA melanoma model. **(b)** Growth curves of the average volumes in the indicated groups (n=8). **(c)** Survival curves of mice with different treatments as indicated (n=8). **(d)** The tumor weight of excised B16-OVA tumors from mice in each group (n=6). **(e)** Tumor inhibition rates are calculated according to the tumor weight (n=6). **(f)** Quantitative analysis of CD3⁺ CD4⁺ T cells. **(g)** CD3⁺ CD8⁺ T cells. **(h)** CD3⁺ CD4⁺ Foxp3⁺ Tregs, and **(i)** MDSCs (CD11b⁺ Gr1⁺). **(j)** Infiltrating the tumor tissues, as examined by flow cytometry (n=3). Flow cytometric analysis assessed IFN-γ⁺ CD4⁺ **(k)** cells and CD8⁺ T **(l)** cells in the tumor tissues of mice in the B16-F10 tumor model. Data are shown as mean ± SD. One-way ANOVA with a Tukey multiple comparisons test was used for statistical analysis. *, p < 0.05; **, p < 0.01; ***, p < 0.001

OVA induced a significant increase in tumor-specific interferon-γ (IFN-γ) secreting CD4⁺ and CD8⁺ T cells (Fig. 6j, k, l). NAPS^{L-p}@OVA treatment also increased CD3⁺ CD4⁺ and CD3⁺ CD8⁺ T cells in the spleen (Supplementary Figs. 30, 31). Tumor tissue histology via H&E staining reveals that among all groups, NAPS^{L-p}@OVA exhibits the lowest cell density, the largest intercellular space, and the most pronounced nucleus atrophy (Supplementary Fig. 32a). Immunofluorescence assays for

CD4 and CD8 markers were conducted. Supplementary Fig. 32b demonstrates that the expressions of CD4 and CD8 are notably elevated in tumor tissues of mice treated with NAPS^{L-p}@OVA, compared to control groups, indicating heightened infiltration of CTLs in tumors prompted by NAPS^{L-p}@OVA. These findings demonstrate that NAPS^{L-p}@OVA effectively activates local and systemic antigen-specific immune responses. The study

highlights the potential of NAPS^{L-p} as a prophylactic and therapeutic vaccine for solid tumors.

NAPS^{L-p}-based vaccination offers strong influenza protection

To test the effectiveness of NAPS^{L-p} in response to H1N1 WIV, mice were immunized subcutaneously with H1N1 WIV alone, NAPS^{L-p} alone, H1N1 WIV plus Al(OH)₃, H1N1 WIV, and NAPS^{L-p} complexes for two doses. Serum samples were collected on days 14, 21, and 28 after the first immunization to measure IgG and hemagglutination-inhibiting (HI) antibody titers (Fig. 7a and b). The H1N1 WIV@NAPS^{L-p} group showed significantly higher IgG and HI titers compared to the H1N1 WIV group on all three-time points ($p < 0.5$ or $p < 0.01$).

To assess the protective efficacy of the H1N1 WIV@NAPS^{L-p} vaccine, mice were intranasally challenged with the H1N1(A/PR/8) virus on day 28 after the initial immunization. Body weight changes and survival rates were monitored for two weeks post-challenge (Fig. 7c and d). Mice immunized with H1N1 WIV@NAPS^{L-p} showed recovery after a slight weight loss, and the survival rate in this group was 88.8%, demonstrating better protection compared to the H1N1 WIV plus Al(OH)₃ group. None of the mice in the H1N1 WIV@NAPS^{L-p} group had detectable virus titers (Fig. 7e). In contrast, mice immunized with H1N1 WIV alone experienced severe weight loss and some died. Lung pathology analysis revealed severe damage in the lungs of mice in the PBS group on day 5 post-infection, including swelling, hyperemia, and hemorrhage. In contrast, mice immunized with H1N1 WIV, H1N1 WIV plus Al(OH)₃, or H1N1 WIV@NAPS^{L-p} showed only slight pathological changes (Fig. 7f, g and Supplementary Fig. 33). These results indicate that vaccination with NAPS^{L-p}-based H1N1 inactivated vaccine protected mice from a lethal influenza challenge.

Discussion

In our study, we discovered a natural polysaccharide with self-assembly properties among 139 bacterial species. Surprisingly, most of these polysaccharides exhibited self-assembly properties and acted as immune adjuvants. These polysaccharides could adopt various nanoscale conformations in solution, such as spherical nanoparticles and nanofibers, which endowed them with multiple functions [30, 31]. The diverse self-assembly properties observed in these polysaccharides can be attributed to variations in molecular weight, residue compositions, and solubility [32]. Based on our SEM, FTIR, and DLS findings, we identified a novel natural polysaccharide from *L.plantarum* with remarkable self-assembly properties. This polysaccharide was named NAPS^{L-p}. Analysis using HPGPC revealed that NAPS^{L-p} is composed of galactosamine hydrochloride, arabinose,

glucosamine hydrochloride, galactose, glucose, mannose, and glucuronic acid. The distinct physical and chemical properties of these carbohydrates contribute to the exceptional self-assembly capabilities of NAPS^{L-p}. As a result, we believe that NAPS^{L-p} exhibits stronger self-assembly abilities compared to other exopolysaccharides, such as those derived from fungus [33], *Klebsiella* EPS of PHRC1.001 [34] and others [35, 36]. NAPS^{L-p} has abundant hydroxyl residues, allowing it to interact with protein antigens through hydrophobic interactions, hydrogen bonding, and electrostatic associations, driving assembly. Research has indicated that the notable immunoreactivity of EPS can be attributed to its chemical constituents, encompassing hydroxyl, carbon radical, and sulfate groups [37, 38]. The strong adjuvant activity of NAPS^{L-p} is attributed to its abundant mannose groups, which readily engage immune receptors [39, 40]. NAPS^{L-p} enhances immune responses by elevating specific serum IgG, IgG1, and IgG2a, which in turn enhances Th1/Th2 response [41]. Moreover, NAPS^{L-p} induces the functional maturation and cross-presentation of DCs by upregulating the expression of molecular markers on DCs surfaces, including CD40, CD80, CD86, and MHC-II, as well as OVA₂₅₇₋₂₆₄ peptide (SIINFEKL)-MHCI. Mature DCs secrete TNF- α , IL-6, and IL-12p70, which enhances Th1 immunity [42]. In contrast, the expression of IL-4 activates the Th2 immune response [43]. Further studies confirmed that NAPS^{L-p} could trigger DC activation and antigen presentation by TLR4 in vitro. However, whether there are other pathways for NAPS^{L-p} still needs further verification. These findings reveal a novel mechanism related to the immune response of NAPS^{L-p} and confirm its potential as an adjuvant for vaccines.

Natural polysaccharides are widespread in organisms from prokaryotes to eukaryotes, serving as critical components involved in various life activities [44, 45]. They have been used for decades as building blocks to create functional biomaterials and can be modified to formulate derivatives for applications in delivery carriers [46, 47]. Additionally, they play essential roles in immune system function and immune response stimulation [48]. Natural polysaccharides possess favorable properties such as biocompatibility, renewability, non-toxicity, biodegradability, and low immunogenicity, making them promising adjuvant candidates [49]. However, obtaining immunopotentiators from natural sources with sufficient quantity, purity, and homogeneity is often challenging [50]. The NAPS^{L-p} that we reported demonstrates high quantity, purity, and homogeneity. It self-assembles into spherical nanoparticles of approximately 30 nm in size, exhibiting brightness and relatively uniform distribution in water. Therefore, we believe NAPS^{L-p} holds promise as a delivery platform.

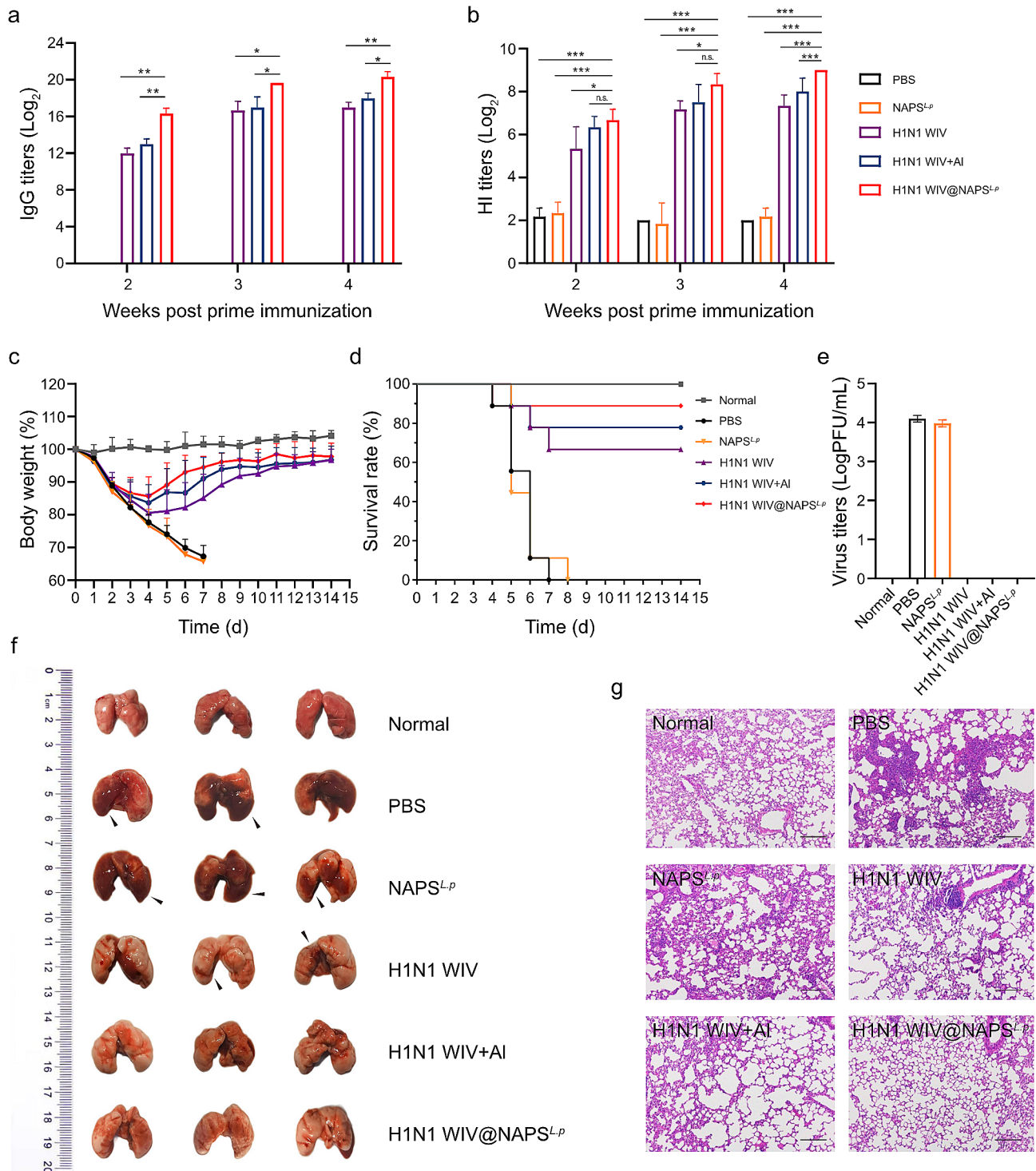


Fig. 7 Immunization with NAPS^{L-p}-based influenza vaccine protects mice against H1N1 influenza virus infection. **(a)** H1N1 WIV-specific serum IgG titers were determined by indirect ELISA. **(b)** Serum hemagglutination inhibition (HI) levels were detected by HI assay using 4 hemagglutinating units of the influenza virus strain. **(c)** Body weight changes in the vaccinated mice were challenged with 10⁶ PFU of H1N1 influenza virus 28 days post-primary immunization. **(d)** Change in the survival of vaccinated mice was challenged with 10⁶ PFU of H1N1 influenza virus 28 days after initial immunization. Mice who lost more than 25% of their body weight were euthanized according to guidelines. $n=9$. **(e)** Virus load in the lung ($n=3$) on day 5 p.i. **(f)** The pathological changes in lungs ($n=3$) on day 5 p.i. **(g)** Representative histopathological changes in H&E-stained lung tissues ($n=3$) on day 5 p.i. magnification 200 \times . Data are shown as mean \pm SD. One-way ANOVA with a Tukey multiple comparisons test was used for statistical analysis. *, $p < 0.05$; **, $p < 0.01$; ***, $p < 0.001$

Recent studies have reported the vaccine adjuvant effects of natural polysaccharides [42, 51]. However, the effectiveness of these polysaccharides as adjuvants is not satisfactory. For instance, the magnitude of RBD-specific antibody responses induced by PRBS-RBD protein nanovaccine was comparable to that of traditional RBD, only around 1.1-fold stronger than the traditional RBD protein vaccine [52]. In contrast, our study demonstrated that NAPS^{L-p}, when used as an immune adjuvant to treat B16-OVA melanoma, exhibited more than a 3.8-fold increase in antibody levels compared to the untreated group, surpassing the performance of Al (OH)₃. Additionally, current research efforts are focused on developing adjuvants that can enhance CD8⁺ T-cell responses and tailored antibody isotypes to improve vaccine responses. Many studies are exploring effective adjuvants and vaccine delivery systems for cancer vaccines [53, 54]. Our nanovaccine elicits immune responses from both CD4⁺ and CD8⁺ T cells and demonstrates excellent preventive effects against melanoma. Furthermore, NAPS^{L-p}-based vaccination showed stronger protective effects against influenza compared to Al (OH)₃ adjuvant.

Our study provides experimental evidence for a new co-assembly polysaccharide with self-assembly properties, optimal antigen packing and presentation, and the ability to induce a persistent anti-tumor immune response, all without the need for crosslinkers or chemical additives. In recent years, there has been a focus on finding safe and effective vaccine adjuvants and drug delivery systems for formulating mucosal vaccines. Natural polysaccharides, with their biocompatibility, biodegradability, non-toxicity, immunological properties, receptor recognition ability for antigen-presenting cells, and cytokine stimulation, hold great potential in this regard. Therefore, natural polysaccharide nanomaterials offer promising prospects for the development of mucosal vaccine adjuvants and delivery systems.

Supplementary Information

The online version contains supplementary material available at <https://doi.org/10.1186/s12951-024-02528-y>.

Supplementary Material 1

Acknowledgements

We thank the State Key Laboratory of State Key Laboratory of Reproductive Regulation & Breeding of Grassland Livestock (Inner Mongolia University) for providing the large-scale instrument-sharing platform. We thank Professor Guojun Wang for help in animal experiments.

Author contributions

S. S. performed all experiments, analyzed data, prepared figures, and wrote the manuscript. H. Z. and X. L. revised figures, and wrote the manuscript. J. C. and P. W. designed the research. Y. L., C. L., H. L., N. P., X. B., and M. N. performed background literature search and review. L. Z., X. L., and P. G. provided technical guidance and experimental guidance. X. W. provided funding and

wrote the manuscript with input from all authors. All authors have approved the final version of the manuscript.

Funding

Research reported in this publication was supported by the Science and Technology Major Project of the Inner Mongolia Autonomous Region of China (grant number 2021ZD0013), Key Scientific and Tech-nonlogical Research Program of Inner Mongolia Autonomous Region (grant number 2021GG0156), and the National Natural Science Foundation of China (grant numbers 32060800).

Data availability

No datasets were generated or analysed during the current study.

Declarations

Ethics approval and consent to participate

All of the animal-related experimental protocols applied in this study were conducted under the standards of the Ethics Committee of Inner Mongolia University (SYXK2020-0006), and executed according to guidelines from the Committee of Welfare and Ethics of Laboratory Animals in Inner Mongolia Province.

Consent for publication

All authors read and approved the final version of this manuscript and agreed to submit it for publication.

Competing interests

The authors declare no competing interests.

Authors' information

Shouxin Sheng, Haochi Zhang, and Xinyu Li equally contribute to this work as first authors.

Received: 9 January 2024 / Accepted: 3 May 2024

Published online: 19 May 2024

References

1. Gay CM, Tong P, Cardnell RJ, Sen T, Su X, Ma J, Bara RO, Johnson FM, Wakefield C, Heymach JV, et al. Differential Sensitivity Analysis for resistant malignancies (DISARM) identifies common candidate therapies across platinum-resistant cancers. *Clin Cancer Res*. 2019;25:346–57.
2. Faccioponte JG, Ugel S, De Sanctis F, Li C, Wang L, Nair G, Sehgal S, Raj A, Matthaiou E, Coukos G, Facciabene A. Tumor endothelial marker 1-specific DNA vaccination targets tumor vasculature. *J Clin Invest*. 2014;124:1497–511.
3. Lycke N. Recent progress in mucosal vaccine development: potential and limitations. *Nat Rev Immunol*. 2012;12:592–605.
4. Vono M, Taccone M, Caccin P, Gallotta M, Donvito G, Falzoni S, Palmieri E, Pallaoro M, Rappuoli R, Di Virgilio F, et al. The adjuvant MF59 induces ATP release from muscle that potentiates response to vaccination. *PNAS*. 2013;110:21095–100.
5. Kim JH, Davis WG, Sambhara S, Jacob J. Strategies to alleviate original antigenic sin responses to influenza viruses. *PNAS*. 2012;109:13751–6.
6. Odunsi K, Matsuzaki J, James SR, Mhawech-Fauceglia P, Tsujii T, Miller A, Zhang W, Akers SN, Griffiths EA, Miliotto A, et al. Epigenetic potentiation of NY-ESO-1 Vaccine Therapy in Human Ovarian Cancer. *Cancer Immunol Res*. 2014;2:37–49.
7. Hornung V, Bauernfeind F, Halle A, Samstad EO, Kono H, Rock KL, Fitzgerald KA, Latz E. Silica crystals and aluminum salts activate the NALP3 inflammasome through phagosomal destabilization. *Nat Immunol*. 2008;9:847–56.
8. Boudreau CM, Yu W-H, Suscovich TJ, Talbot HK, Edwards KM, Alter G. Selective induction of antibody effector functional responses using MF59-adjuvanted vaccination. *J Clin Invest*. 2020;130:662–72.
9. Sun B, Ji Z, Liao Y-P, Wang M, Wang X, Dong J, Chang CH, Li R, Zhang H, Nel AE, Xia T. Engineering an effective Immune adjuvant by designed control of shape and crystallinity of Aluminum Oxyhydroxide nanoparticles. *ACS Nano*. 2013;7:10834–49.
10. Serradell MC, Rupil LL, Martino RA, Prucca CG, Carranza PG, Saura A, Fernández EA, Gargantini PR, Tenaglia AH, Petiti JP, et al. Efficient oral vaccination

- by bioengineering virus-like particles with protozoan surface proteins. *Nat Commun.* 2019;10:361.
11. Didierlaurent AM, Laupèze B, Di Pasquale A, Hergli N, Collignon C, Garçon N. Adjuvant system AS01: helping to overcome the challenges of modern vaccines. *Expert Rev Vaccines.* 2017;16:55–63.
 12. Sobolev O, Binda E, O'Farrell S, Lorenc A, Pradines J, Huang Y, Duffner J, Schulz R, Cason J, Zambon M, et al. Adjuvanted influenza-H1N1 vaccination reveals lymphoid signatures of age-dependent early responses and of clinical adverse events. *Nat Immunol.* 2016;17:204–13.
 13. Wang T, Upponi JR, Torchilin VP. Design of multifunctional non-viral gene vectors to overcome physiological barriers: dilemmas and strategies. *Int J Pharm.* 2012;427:3–20.
 14. Lavelle EC, Ward RW. Mucosal vaccines - fortifying the frontiers. *Nat Rev Immunol.* 2022;22:236–50.
 15. Negahdaripour M, Golkar N, Hajjghahramani N, Kianpour S, Nezafat N, Ghasemi Y. Harnessing self-assembled peptide nanoparticles in epitope vaccine design. *Biotechnol Adv.* 2017;35:575–96.
 16. Singh B, Maharjan S, Cho K-H, Cui L, Park I-K, Choi Y-J, Cho C-S. Chitosan-based particulate systems for the delivery of mucosal vaccines against infectious diseases. *Int J Biol Macromol.* 2018;110:54–64.
 17. De Koker S, De Geest BG, Singh SK, De Rycke R, Naessens T, Van Kooyk Y, Demeester J, De Smedt SC, Grooten J. Polyelectrolyte microcapsules as Antigen Delivery vehicles to dendritic cells: Uptake, Processing, and Cross-presentation of Encapsulated antigens. *Angew Chem Int Ed.* 2009;48:8485–9.
 18. Nembrini C, Stano A, Dane KY, Ballester M, van der Vlies AJ, Marsland BJ, Swartz MA, Hubbell JA. Nanoparticle conjugation of antigen enhances cytotoxic T-cell responses in pulmonary vaccination. *PNAS.* 2011;108:E989–97.
 19. Truffi M, Fiandra L, Sorrentino L, Monieri M, Corsi F, Mazzucchelli S. Ferritin nanocages: a biological platform for drug delivery, imaging and therapeutics in cancer. *Pharmacol Res.* 2016;107:57–65.
 20. Huang Y, Wang Y-J, Wang Y, Yi S, Fan Z, Sun L, Lin D, Anreddy N, Zhu H, Schmidt M, et al. Exploring naturally occurring ivy nanoparticles as an alternative biomaterial. *Acta Biomater.* 2015;25:268–83.
 21. Thomann-Harwood LJ, Kaeuper P, Rossi N, Milona P, Herrmann B, McCullough KC. Nanogel vaccines targeting dendritic cells: contributions of the surface decoration and vaccine cargo on cell targeting and activation. *J Control Release.* 2013;166:95–105.
 22. Mallakpour S, Azadi E, Hussain CM. Chitosan, alginate, hyaluronic acid, gums, and β -glucan as potent adjuvants and vaccine delivery systems for viral threats including SARS-CoV-2: a review. *Int J Biol Macromol.* 2021;182:1931–40.
 23. Honda-Okubo Y, Saade F, Petrovsky N. Advax™, a polysaccharide adjuvant derived from delta inulin, provides improved influenza vaccine protection through broad-based enhancement of adaptive immune responses. *Vaccine.* 2012;30:5373–81.
 24. Alameh M, Lavertu M, Tran-Khanh N, Chang C-Y, Lesage F, Bail M, Darras V, Chevrier A, Buschmann MD. siRNA delivery with Chitosan: influence of Chitosan Molecular Weight, Degree of Deacetylation, and Amine to phosphate ratio on in vitro silencing efficiency, Hemocompatibility, Biodistribution, and in vivo efficacy. *Biomacromolecules.* 2018;19:112–31.
 25. Jiang H-L, Park I-K, Kang M-L, Yoo H-S, Choi Y-J, Akaike T, Cho C-S. Immune stimulating activity of an atrophic rhinitis vaccine associated to pegylated chitosan microspheres in vitro. *Polym Adv Technol.* 2007;18:220–5.
 26. Shi G-N, Zhang C-N, Xu R, Niu J-F, Song H-J, Zhang X-Y, Wang W-W, Wang Y-M, Li C, Wei X-Q, Kong D-L. Enhanced antitumor immunity by targeting dendritic cells with tumor cell lysate-loaded chitosan nanoparticles vaccine. *Biomaterials.* 2017;113:191–202.
 27. Khormaee S, Choi Y, Shen MJ, Xu B, Wu H, Griffiths GL, Chen R, Slater NKH, Park JK. Endosomolytic anionic polymer for the cytoplasmic delivery of siRNAs in localized in vivo applications. *Adv Funct Mater.* 2013;23:565–74.
 28. Guo S, Huang Y, Jiang Q, Sun Y, Deng L, Liang Z, Du Q, Xing J, Zhao Y, Wang PC, et al. Enhanced gene delivery and siRNA silencing by gold nanoparticles coated with Charge-Reversal Polyelectrolyte. *ACS Nano.* 2010;4:5505–11.
 29. Zhang G, Fu X, Sun H, Zhang P, Zhai S, Hao J, Cui J, Hu M. Poly(ethylene glycol)-Mediated assembly of vaccine particles to Improve Stability and Immunogenicity. *ACS Appl Mater Interfaces.* 2021;13:13978–89.
 30. Kianpour S, Ebrahimezhad A, Negahdaripour M, Mohkam M, Mohammadi F, Niknezhad SV, Ghasemi Y. Characterization of biogenic Fe (III)-binding exopolysaccharide nanoparticles produced by *Ralstonia* sp. SK03. *Biotechnol Prog.* 2018;34:1167–76.
 31. Rolandi M, Rolandi R. Self-assembled chitin nanofibers and applications. *Adv Colloid Interface Sci.* 2014;207:216–22.
 32. Fan Y, Liu Y, Wu Y, Dai F, Yuan M, Wang F, Bai Y, Deng H. Natural polysaccharides based self-assembled nanoparticles for biomedical applications – A review. *Int J Biol Macromol.* 2021;192:1240–55.
 33. Xu S, Xu X, Zhang L. Branching structure and chain conformation of Water-Soluble Glucan extracted from *Auricularia auricula-judae*. *J Agric Food Chem.* 2012;60:3498–506.
 34. Zhao M, Cui N, Qu F, Huang X, Yang H, Nie S, Zha X, Cui SW, Nishinari K, Phillips GO, Fang Y. Novel nano-particulated exopolysaccharide produced by *Klebsiella* sp. PHRC1.001. *Carbohydr Polym.* 2017;171:252–8.
 35. Charoenwongpaiboon T, Wangpaiboon K, Pichyangkura R, Nepogodiev SA, Wonganan P, Mahalapbutr P, Field RA. Characterization of a nanoparticulate exopolysaccharide from *Leuconostoc holzapfelii* KM01 and its potential application in drug encapsulation. *Int J Biol Macromol.* 2021;187:690–8.
 36. Li C, Zhou L, Yang H, Lv R, Tian P, Li X, Zhang Y, Chen Z, Lin F. Self-assembled Exopolysaccharide nanoparticles for Bioremediation and Green Synthesis of Noble Metal Nanoparticles. *ACS Appl Mater.* 2017;9:22808–18.
 37. Pyclick M, Srutkova D, Schwarzer M, Górska S. Bifidobacteria cell wall-derived exo-polysaccharides, lipoteichoic acids, peptidoglycans, polar lipids and proteins – their chemical structure and biological attributes. *Int J Biol Macromol.* 2020;147:333–49.
 38. Zhu S, Han J, Yan Z, Wu Y, Zhang W, Xia W, Feng H. Structure elucidation and immunological activity of a novel exopolysaccharide from *Paenibacillus bovis* sp. nov. BD3526. *Carbohydr Polym.* 2022;282:119103.
 39. Figueiredo RT, Bittencourt VCB, Lopes LCL, Sassaki G, Barreto-Bergter E. Toll-like receptors (TLR2 and TLR4) recognize polysaccharides of *Pseudallescheria boydii* cell wall. *Carbohydr Res.* 2012;356:260–4.
 40. Chen R, Xu J, Wu W, Wen Y, Lu S, El-Seedi HR, Zhao C. Structure-immunomodulatory activity relationships of dietary polysaccharides. *Curr Res Food Sci.* 2022;5:1330–41.
 41. Li Q, Weng X, Zhao B, Yang Y, Zhang A. Immunoregulatory properties of the cultivated *Artemisia rupestris* L. polysaccharide as a potential adjuvant. *Carbohydr Polym.* 2022;291:119525.
 42. Pi C-C, Chu C-L, Lu C-Y, Zhuang Y-J, Wang C-L, Yu Y-H, Wang H-Y, Lin C-C, Chen C-J. Polysaccharides from *Ganoderma formosanum* function as a Th1 adjuvant and stimulate cytotoxic T cell response in vivo. *Vaccine.* 2014;32:401–8.
 43. Ochi A, Nguyen AH, Bedrosian AS, Mushlin HM, Zerbakhsh S, Barilla R, Zambirinis CP, Fallon NC, Rehman A, Pylayeva-Gupta Y, et al. MyD88 inhibition amplifies dendritic cell capacity to promote pancreatic carcinogenesis via Th2 cells. *J Exp Med.* 2012;209:1671–87.
 44. Jin M, Shi J, Zhu W, Yao H, Wang DA. Polysaccharide-based biomaterials in tissue Engineering: a review. *Tissue Eng Part B Rev.* 2021;27:604–26.
 45. Li X, Zhang Z-H, Qi X, Li L, Zhu J, Brennan CS, Yan J-K. Application of nonthermal processing technologies in extracting and modifying polysaccharides: a critical review. *Compr Rev Food Sci Food Saf.* 2021;20:4367–89.
 46. Fakhri E, Eslami H, Maroufi P, Pakdel F, Taghizadeh S, Ganbarov K, Yousefi M, Tanomand A, Yousefi B, Mahmoudi S, Kafil HS. Chitosan biomaterials application in dentistry. *Int J Biol Macromol.* 2020;162:956–74.
 47. Dheer D, Arora D, Jaglan S, Rawal RK, Shankar R. Polysaccharides based nanomaterials for targeted anti-cancer drug delivery. *J Drug Target.* 2017;25:1–16.
 48. Dacoba TG, Omange RW, Li H, Crecente-Campo J, Luo M, Alonso MJ. Polysaccharide nanoparticles can efficiently modulate the immune response against an HIV peptide Antigen. *ACS Nano.* 2019;13:4947–59.
 49. Jin Z, Gao S, Cui X, Sun D, Zhao K. Adjuvants and delivery systems based on polymeric nanoparticles for mucosal vaccines. *Int J Pharm.* 2019;572:118731.
 50. Sun B, Yu S, Zhao D, Guo S, Wang X, Zhao K. Polysaccharides as vaccine adjuvants. *Vaccine.* 2018;36:5226–34.
 51. Wattanasiri C, Paha J, Ponpuak M, Ruchirawat S, Boonyarattanakalin S. Synthesis of synthetic mannan backbone polysaccharides found on the surface of *Mycobacterium tuberculosis* as a vaccine adjuvant and their immunological properties. *Carbohydr Polym.* 2017;175:746–55.
 52. Chen S, Yang L, Ou X, Li J-Y, Zi C-T, Wang H, Hu J-M, Liu Y. A new polysaccharide platform constructs self-adjuvant nanovaccines to enhance immune responses. *J Nanobiotechnol.* 2022;20:320.
 53. van Kooyk Y, Rabinovich GA. Protein-glycan interactions in the control of innate and adaptive immune responses. *Nat Immunol.* 2008;9:593–601.

54. Hameed SA, Paul S, Dellosa GKY, Jaraquemada D, Bello MB. Towards the future exploration of mucosal mRNA vaccines against emerging viral diseases; lessons from existing next-generation mucosal vaccine strategies. *NPJ Vaccines*. 2022;7:71.

Publisher's Note

Springer Nature remains neutral with regard to jurisdictional claims in published maps and institutional affiliations.